Clay Minerals (2020), **55**, 71–82
doi:10.1180/clm.2020.12

CAMBRIDGE UNIVERSITY PRESS

Article

Mineralogical and hydraulic characteristics of mudstone in the Tamusu candidate area in northwest China for high-level radioactive waste geological disposal

Long Xiang[1,2], Xiaodong Liu[1,2*], Pinghui Liu[1,2], Xingfu Jiang[1,2] and Chaocheng Dai[1,2]

[1]College of Earth Sciences, East China University of Technology, Nanchang 330013, China and [2]State Key Laboratory of Nuclear Resources and Environment, East China University of Technology, Nanchang 330013, China

Abstract

The Tamusu region in northwest China is a key candidate area for China's clay rock deep geological repositories (DGRs) for high-level radioactive waste (HLRW) as it is composed of a continuous layer of thick lacustrine mudstone. To evaluate this mudstone as a host rock, two special test boreholes were drilled to investigate its spatial distribution and mineralogical and hydraulic characteristics. The southwest boundary and depositional centre of the lake basin were well delineated by boreholes TZK-1 and TZK-2. The continuous single-layer thickness of the target mudstone formation was up to 300 m at a depth of 500–800 m. Three main mineral types were determined, namely carbonates (mainly dolomite and ankerite), analcime and albite, and their abundance was used to distinguish three different facies. Other mineral phases, such as clay minerals (mainly illite and kaolinite), pyrite, hematite, quartz and calcite, were present as admixtures. The presence of carbonates may increase the mechanical strength and analcime may enhance the radionuclide adsorption properties of the mudstone. The self-sealing properties, which may be affected by the small amount of clay minerals, remain to be investigated. The hydraulic conductivity of the mudstone determined via *in situ* pulse tests ranged from 10^{-13} to 10^{-10} m s^{-1}, suggesting that the Tamusu mudstone has ultra-low permeability. The transmissivity of the Tamusu mudstone fluctuated in regions with varying lithologies, but remained relatively constant for consistent lithologies. In summary, these preliminarily results confirm the possible suitability of the target formation as a host rock for DGRs of China's HLRW.

Keywords: geological disposal, high-level radioactive waste, HLRW, hydraulic characteristics, mudstone characteristics, Tamusu area

(Received 25 July 2019; revised 17 April 2020; Accepted Manuscript online: 4 May 2020; Associate Editor: Stephan Kaufhold)

Deep geological repositories (DGRs) have been accepted internationally for the permanent disposal of high-level radioactive waste (HLRW) (IAEA, 1997, 2003; Pan & Qian, 2009; McEvoy *et al.*, 2016). They typically rely on a multi-barrier system consisting of a natural geological barrier and an engineered barrier system (SKB, 2004; Zhang, 2006). As the natural geological barrier (*i.e.* the host rock) plays a critical role in ensuring the long-term safety of DGRs, several types of rocks have been considered as potential host rocks for DGRs, including granite, clay rocks, rock salt, tuffs and crystalline rocks in general (NEA, 2001; Yoshida *et al.*, 2014; McMaster *et al.*, 2018). Granite has been considered as a potential host rock for the DGRs in Sweden, Finland and China (Delay *et al.*, 2010; Hudson *et al.*, 2011; Wang *et al.*, 2018).

Clay rocks are widely accepted as potential host rocks for DGRs due to their attractive properties, such as large rock mass, stable geological structure, low hydraulic conductivity, self-sealing potential of fractures and high sorption capacity for radionuclides (Zhang, 2018). Many studies have focused on the properties of clay rock, such as mineralogical composition (Gaucher *et al.*, 2004; Zhang, 2018), water contents and permeability (Andra, 2005; Delay, 2006; Distinguin & Lavanchy, 2007), safety as a repository (Mazurek *et al.*, 2008; Cuss *et al.*, 2014; Sasamoto *et al.*, 2017) and effects of the clay types on bentonite (Kohno *et al.*, 2018; Matusewicz & Olin, 2019), which may be used as an additional barrier. France and Switzerland plan to construct repositories in Callovo-Oxfordian (COX) clay and Opalinus (OPA) clay formations at depths of 420–550 m and 400–700 m below surface, respectively (NAGRA, 2002; Andra, 2015).

In 2009, nationwide screening started for clay rock sites in mainland China. Since then, four regions have been preliminarily identified as potential clay rock DGR candidate sites: (1) the Tamusu and (2) Suhongtu areas in the Inner Mongolia Autonomous Region; (3) the Longdong area in Guansu Province; and (4) the Nanbaxian area in the northwest of Qaidam Basin (Fig. 1a). In addition, basic criteria for the site selection of clay rock repositories in China have been developed by referencing standards from the International Atomic Energy Agency (IAEA) and experiences abroad (IAEA, 1997, 2003; Andra, 2005; Pan & Qian, 2009; Liu *et al.*, 2012). Based on the results of preliminary evaluations of socioeconomic conditions (Liu & Liu, 2012; Guan *et al.*, 2014; Yang, *et al.*, 2017) and basic mechanical properties (Wang *et al.*, 2018), the Tamusu area might be considered as a key candidate area for establishing a clay rock DGR.

In this paper, the suitability of the target mudstone formation in the Tamusu region is discussed in the context of the results obtained from two test boreholes (borehole TZK-1 and borehole

*E-mail: liuof99@163.com

Cite this article: Xiang L, Liu X, Liu P, Jiang X, Dai C (2020). Mineralogical and hydraulic characteristics of mudstone in the Tamusu candidate area in northwest China for high-level radioactive waste geological disposal. *Clay Minerals* **55**, 71–82. https://doi.org/10.1180/clm.2020.12

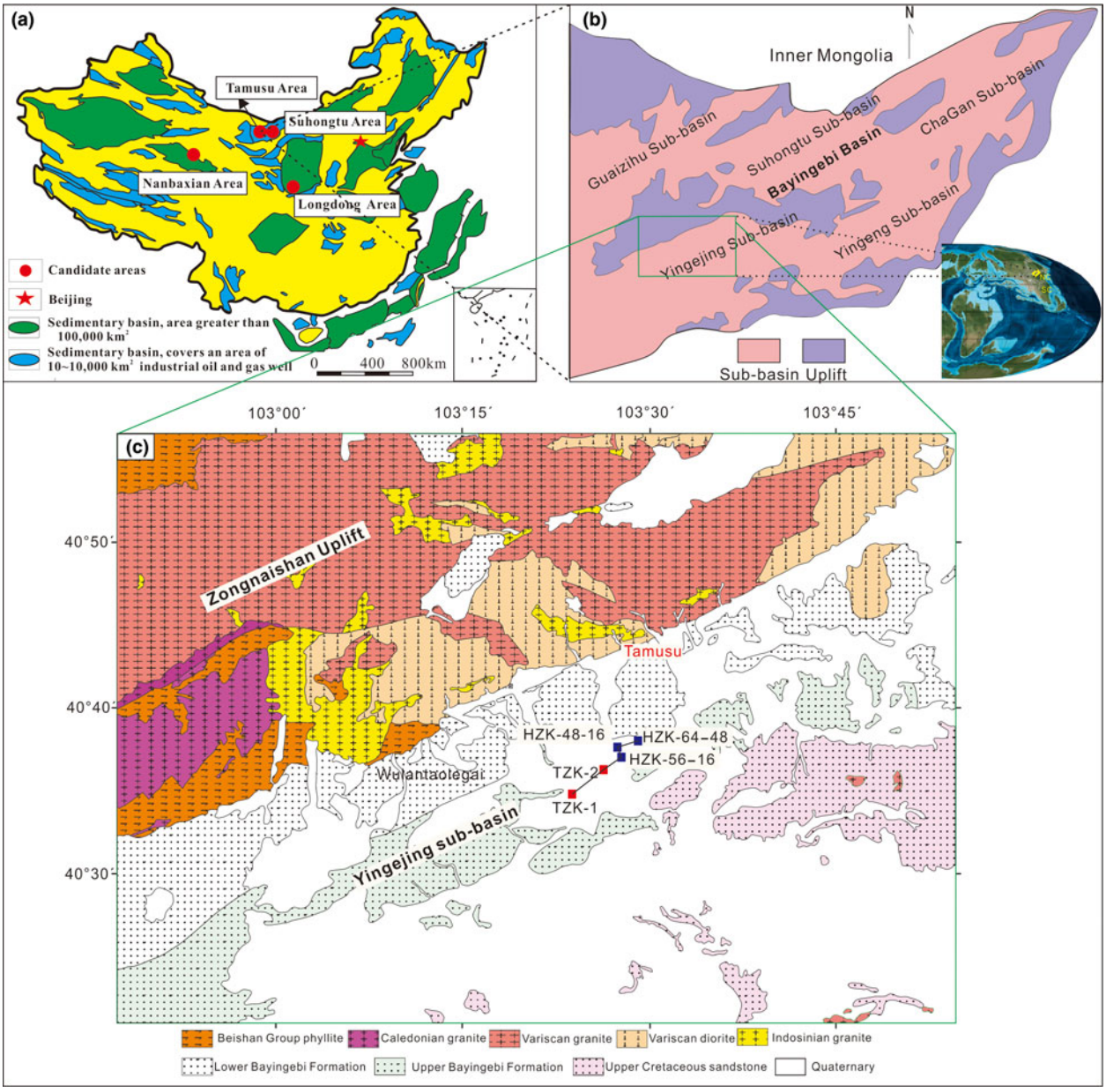

Fig. 1. (a) Location of the four preliminary candidate areas (after Liu *et al.*, 2010). (b) The Cretaceous palaeogeography shows that the Bayingebi Basin is located in the orogenic zone between the Siberian and the North China blocks in the temperature zone. (c) Geological map of the Yingejing Sub-basin and borehole locations. The boreholes indicated by the red squares were drilled by the present team, whereas those indicated by the blue squares were drilled by Geological Team No. 208 (Wei & Jiang, 2019).

TZK-2) drilled in the area. The following topics are presented: (1) analysis of the spatial distribution of the characteristics of the target mudstone (geological homogeneity); (2) analysis of mineralogical characteristics; (3) analysis of *in situ* testing of the hydraulic conductivity via pulse tests; and (4) discussion of the suitability of the target formation as a host rock for DGR purposes.

Geological setting

The Bayingebi Basin

The Bayingebi Basin (Inner Mongolia, northwest China) is located in the southern margin of the Xingmeng Orogenic Belt (Lin *et al.*, 2001; Dou & Chang, 2003) in the Eastern Central Asian Orogenic Zone (Zhou *et al.*, 2010), which is framed by the Siberian Craton and the North China Craton (Fig. 1b) (Charles *et al.*, 2013). This basin is a Mesozoic terrestrial rift basin that developed on the Palaeozoic fold basement and Precambrian crystalline bedrock (Wei *et al.*, 2006; Wei & Jiang, 2019). The basement is composed primarily of Palaeozoic and early Mesozoic intermediate to felsic granitic plutons, mafic to felsic volcanic rocks and Proterozoic to Palaeozoic sedimentary or metasedimentary units (Meng *et al.*, 2002; Zhang *et al.*, 2019). Triassic and Jurassic strata are only distributed in the northwest area of the basin and consist of fluvial and lacustrine sandstone, shale, mudstone and coal seams. The Cretaceous strata are divided into the Bayingebi, Suhongtu, Yingen and Wulansuhai formations. Cenozoic strata (alluvial and fluvial

https://doi.org/10.1180/clm.2020.12 Published online by Cambridge University Press

deposits) occur sporadically, and Cretaceous strata represent the main sedimentary covering of all sub-basins in the basin, which are composed of alluvial fans and lacustrine facies (consisting of conglomerates, sandstone, shale and sandy limestone).

Target formation

The Tamusu area, a key clay rock DGR candidate area for China's HLRW, is located in the northeast margin of the Yingejing sub-basin. The sub-basin is framed by the Zongnaishan and the Bayannuoergong uplifts, with northeast–southwest orientation (Fig. 1c). The Early Cretaceous Bayingebi formation is divided into the lower Bayingebi formation (K_1b^1) and the upper Bayingebi formation (K_1b^2) (Zhang *et al.*, 2019). Alluvial fan and fan delta systems developed mostly in the lower Bayingebi formation, consisting of red detrital rocks that underwent a maximum burial depth of ~1400 m. The sedimentary rocks of the upper Bayingebi formation contain sediments typical of alluvial fan, fan delta, braided delta and well-developed lacustrine facies. The target mudstone formation consists of a set of grey lacustrine mudstones comprising the upper Bayingebi formation (K_1b^2), which was identified at a maximum depth of ~911 m.

Based on boreholes drilled earlier by Geologic Party No. 208 in the northeast of the sub-basin (Fig. 1c) and sedimentary research (Wu *et al.*, 2010; Deng, 2013; Li, 2018; Wang *et al.*, 2018), the lacustrine, fan delta and braided delta facies comprise the upper Bayingebi formation. The target formation (K_1b^2) consists of a succession of mudstone–sandstone–mudstone (Wang *et al.*, 2018). The lower mudstone unit is mainly composed of a grey–greyish white mudstone deposited in a semi-deep to deep lacustrine environment. The second sandstone unit comprises yellowish-brown sandstone, siltstone and grey mudstone, representing fan delta and braided delta plain sub-facies (Wu *et al.*, 2010). The third lithological unit is a thick grey–dark grey mudstone, which was formed in a semi-deep to shallow lacustrine environment. To delineate the southwest margin of the lacustrine basin and to define the occurrence of the target formation in the Tamusu area, the boreholes TZK-1 and TZK-2 were drilled between June and August 2017. This was the first time that test boreholes were drilled in the Tamusu area to conduct evaluations on the suitability of clay rock DRGs for China's HLRW. Borehole TZK-1, located in the southwest of the Tamusu area, contributed significantly to delineating the southwest margin of the lacustrine basin. The core lithology highlights the interbedded mudstone–sandstone–mudstone structure of the target formation (Fig. 2), which indicates that the depositional centre of the lacustrine basin is probably located in the northeast. In particular, the first unit with a maximum depth of ~200 m consists primarily of fine-grained sandstone and silty mudstone with thin argillaceous siltstone beds. The fine-grained sandstone is characterized by a massive structure and parallel bedding with a reddish-brown colour. The second unit (200–450 m) is composed mainly of interbedded fine-grained sandstones and argillaceous siltstone. The third unit (450–800 m) consists of dark grey mudstone (Fig. 2). Based on the lithological characteristics of the samples from borehole TZK-1 and earlier drilled boreholes (Fig. 1), borehole TZK-2 was drilled to explore the potential depositional centre of the lacustrine basin and the continuous thickness of the mudstone. The entire target formation consists of dark grey mudstone, which indicates that borehole TZK-2 was located close to the depositional centre of the lacustrine basin.

Materials and methods

Mineralogical analysis

Core samples were collected every 3 m in the field at depths between 381.82 and 800.60 m. A total of 116 core samples from borehole TZK-2 were vacuum sealed to maintain freshness. Then, the whole-rock samples were powdered to pass through a 200 mesh sieve prior to testing. Conventional X-ray diffraction (XRD) analysis was carried out on whole-rock powdered samples with Cu-*K*α radiation operating at 40 mA and 40 kV (D8 ADVANCE, Bruker, Germany). Diffraction traces were recorded from 5 to 70°2θ and the semi-quantitative estimates of relative mass fractions were calculated using the Bruker *Diffrac.EVA* package. This method provides a semi-quantitative analysis, which, in the case of significant differences in the compositions of the samples, may provide meaningful values with an average precision of ~5%. These tests were completed in the State Key Laboratory of Nuclear Resources and Environment, East China University of Technology, China. To characterize the clay mineralogy, the clay fractions (<2 μm) of the samples were investigated using oriented mounts in the air-dried state after ethylene glycol solvation and after heating at 495°C. The preparation of the oriented mounts was conducted in the GeoResources Laboratory of the University of Lorraine, France. The XRD traces were recorded with Cu-*K*α radiation operating at 2.2 kW using a D2 ADVANCE Bruker diffractometer. Diffraction patterns were recorded from 2 to 30°2θ and clay mineral relative contents were calculated based on ethylene glycol patterns and on Thierry (1985). An absolute uncertainty of ± 5% remains even if many characteristic parameters of the minerals to be quantified are known (Reynolds, 1989). Dolomite and ankerite are difficult to distinguish by XRD, so a polarizing microscope in combination with alizarin red-S etching (Li *et al.*, 2012) was applied by the Langfang (China) Shangyi Rock Mine Detection Technology Service Co., Ltd for this purpose. Structural characteristics and major minerals were investigated using a polarizing microscope.

Measurement of hydraulic conductivity

At the conclusion of the drilling stage, the hydraulic conductivities of boreholes TZK-1 and TZK-2 were tested *in situ* with pulse tests conducted using a heavy-duty double-packer (HDDP) system, which was operated with the help of the Beijing Research Institute of Uranium Geology (BRIUG). The HDDP system (Solexperts, Switzerland) consists of four independent components: equipment installed in the borehole; a data-acquisition unit; a water-stop packer pressure-control unit; and a flow-control unit (Fig. 3). In the HDDP system, the two water-stop packers could be pressurized or decompressed independently, which allowed a single packer test to be conducted while the other was pressurized. As a result, the mode of operation could be switched independently between double and single water-stop packer modes without the need to remove any of the down-hole devices. The data from the pulse test were curve-fitted using the *Hytool* analytical software.

Results and discussion

Mineralogical characterization of mudstone

Microscopic analysis

The mudstone samples from the two boreholes contained typical structures, including stockwork, massive, 'porphyritic-like' and lamellar structures. In particular, the stockwork structure is characterized by thick, white, irregular strips connected by white veins that

https://doi.org/10.1180/clm.2020.12 Published online by Cambridge University Press

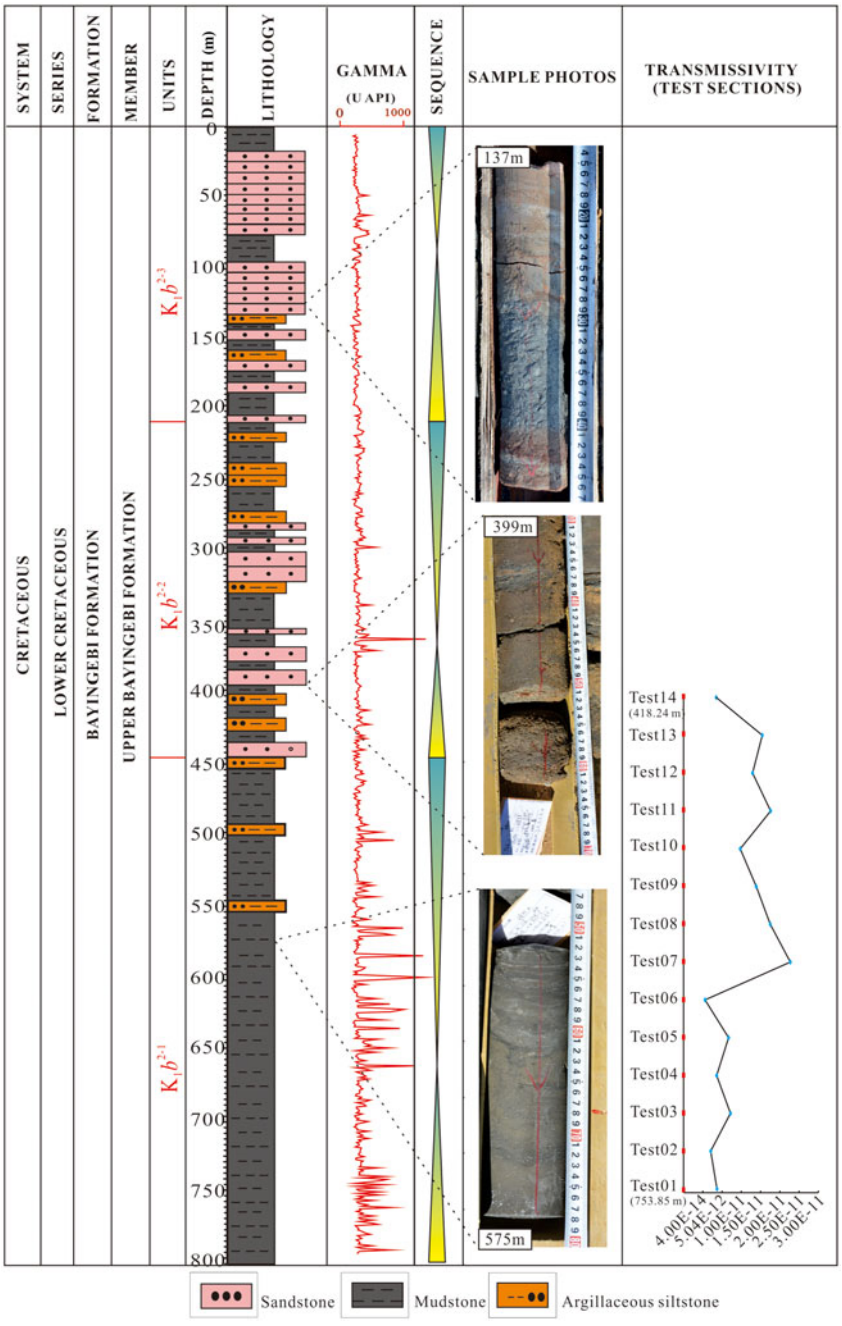

Fig. 2. Lithology and transmissivity of borehole TZK-1.

exhibit an interlaced reticular structure 1–6 mm in width (Fig. 4a). The white stockwork and veins are composed primarily of dolomite, ankerite, analcime and microcrystalline calcite mixed with dark argillite (Fig. 4b). The 'porphyritic-like' structure resembles a 'snowflake' in dark grey mudstone (Fig. 4c), and the typical rhombohedral coarse-grained dolomite is surrounded by dark argillite with particle sizes ranging from 0.5 to 1.0 mm (Fig. 4d). As the primary structure in the target formation, the massive structure is grey and dark grey, apparently homogeneous and highly consolidated (Fig. 4e). The laminar structures have thicknesses varying from 1 to 3 cm (Fig. 4f). Under plane polarized light, etched thin sections (alizarin red-S and potassium ferricyanide solution dyeing) appeared dark blue for ankerite, beige for coarse dolomite (undifferentiated) and grey–white for analcime with negative relief (Fig. 4g). It is worth noting that a high-angled gypsum interlayer was identified at a depth of 300 m in borehole TZK-2 (Fig. 4h).

XRD analyses

The target mudstone formation is mainly composed of three mineral species: carbonates (dolomite and ankerite), albite and analcime. In addition, small amounts of evenly distributed clay minerals (mainly illite and kaolinite), quartz, calcite, hematite and pyrite are also present. Typical whole-rock XRD traces of two samples (T44 and T126) are shown in Fig. 5.

Carbonate minerals are abundant in all samples. In particular, the mass fractions of dolomite and ankerite ranged from 3 to 50% and from 4 to 25%, respectively, with average mass fractions of 28% and 13%, respectively. The mass

https://doi.org/10.1180/clm.2020.12 Published online by Cambridge University Press

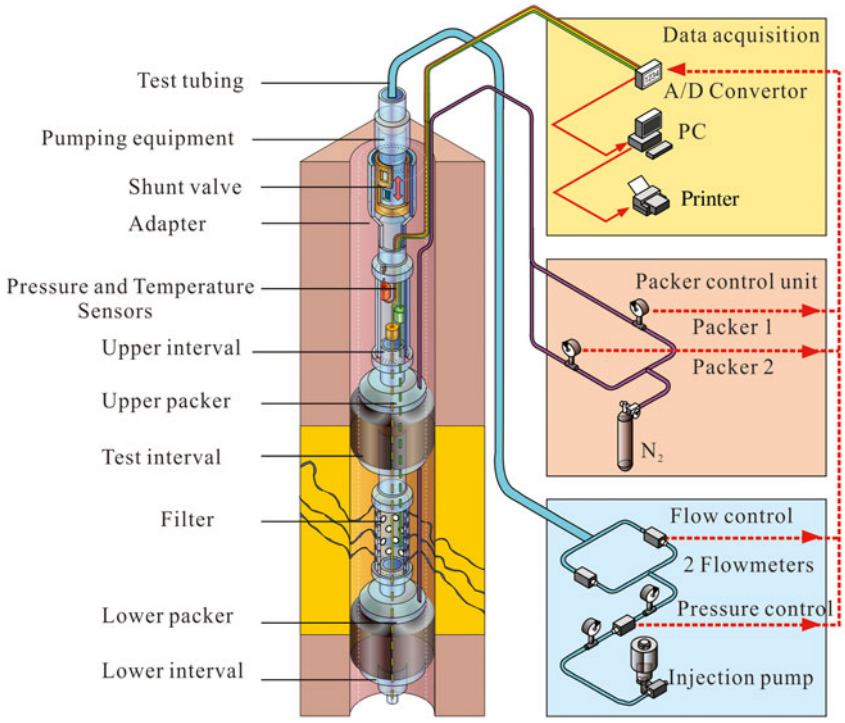

Fig. 3. Technical setup of the HDDP system.

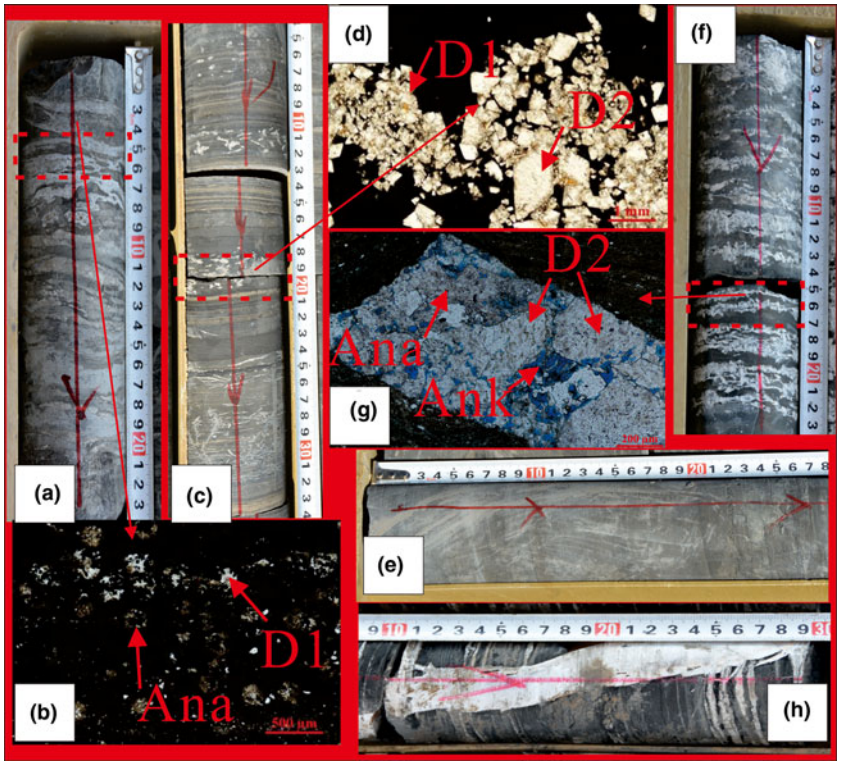

Fig. 4. Typical structures in the Tamusu mudstone. (a) Stockwork structure, with marked white veinlets composed of analcime and dolomite, borehole TZK-2, 765 m. (b) Dark argillaceous structures mixed with evenly distributed powder-fine dolomite and analcime, plane polarized light. (c) 'Porphyritic-like' structure, marked large, white particles composed of fine-grained and coarse-grained dolomite in a fine-grained matrix, borehole TZK-1, 595 m. (d) Rhombic coarse-grained dolomite and fine-grained dolomite crystals are distributed in a dark clay matrix, plane polarized light. (e) Massive structure, borehole TZK-1, 520 m. (f) White and grey–white laminae developed in dark grey mudstone. (g & f) The marked regions are composed of dolomite, ankerite and analcime, borehole TZK-2, 137 m, dyed thin, plane polarized light. (h) Gypsum-containing mudstone, TZK-2, 144 m. Ana = analcime; Ank = ankerite; D1 = powder-fine dolomite; D2 = coarse-grained dolomite.

fractions of analcime and calcite ranged from 1% to 43% and from 0.2% to 23%, respectively, with averages of 17% and 3%, respectively. Both analcime and calcite decreased rapidly with depth. The mass fractions of albite, quartz, hematite and pyrite were evenly distributed and ranged from 7 to 40%, 1 to 11%, 1 to 9% and 2 to 20%, respectively, with average values of 19%, 5%, 4% and 6%, respectively. The mass fractions of illite and kaolinite ranged from 2 to 6% and from 1 to 4%, respectively, with average mass fractions of 3% and 2%, respectively. In addition, the relative abundances of clay minerals after ethylene glycol solvation were investigated preliminarily (Fig. 6). T1 (at 50 m depth, TZK-2) is composed of illite (63%), kaolinite

https://doi.org/10.1180/clm.2020.12 Published online by Cambridge University Press

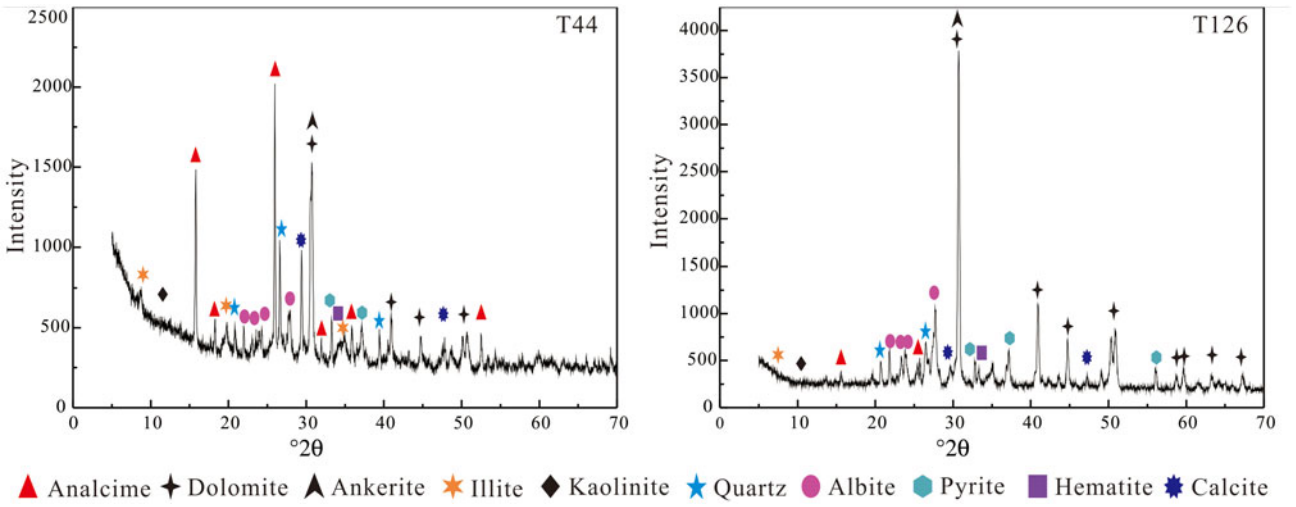

Fig. 5. XRD traces of typical whole-rock samples.

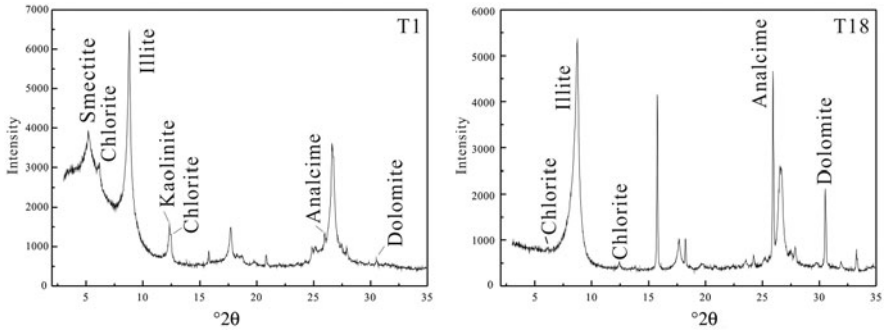

Fig. 6. Oriented XRD traces of ethylene glycol-solvated <2 μm clay fractions of the T1 and T18 samples.

(8%), chlorite (7%) and smectite (22%), and T18 (at 515 m depth, TZK-2) is composed of illite (96%) and chlorite (4%), confirming that the main clay mineral is illite. Analcime and dolomite were also detected in the clay fractions, suggesting a small particle size for these minerals.

Based on the whole-rock mineralogical analysis of 116 samples, three facies could be distinguished (Fig. 7). The first facies (381.82–528.77 m, above Line E–F) is composed mainly of analcime, carbonate minerals and albite, with analcime being the most abundant. The second facies (528.77–723.79 m, between Line E–F and Line M–N) consists mainly of carbonate minerals, analcime and albite. The third facies (723.79–800.06 m, below Line M–N) is composed mainly of carbonate minerals and albite, showing the smallest analcime content.

Shale classification triangles (Zhong *et al.*, 2018) were applied to compare the Tamusu mudstone with other target DGR rocks (Fig. 8). The COX and OPA clays have various clay/carbonate ratios. In contrast, the clay content of the Tamusu mudstone is low. However, if analcime is considered instead of clay minerals in the triangle plot, the analcime/carbonate ratio determines the mineralogical variability of the Tamusu mudstone, in analogy to COX and OPA clays (Zhong *et al.*, 2018). No data points were observed in the siliceous mudstone area (area E, Fig. 8). The COX clay and Tamusu mudstone are mainly characterized as mixed mudstones (area D1, Fig. 8), with the clay mineral content being generally higher in OPA clays. The triangular diagram does not reflect the type of carbonate, which may be used for additional characterization. The carbonate minerals of Tamusu mudstone are dominated by dolomite and ankerite, whereas calcite dominates in COX and OPA clays. Overall, the Tamusu mudstone, in contrast to COX and OPA clays, contains zeolites that may play a role with respect to radionuclide retention, as discussed in the case of the Yucca Mountain potential host rock (Bish, 1999) and for low- and intermediate-level short-lived radioactive waste in Belgium (Misaelides, 2019). The large carbonates contents may affect the mechanical stability positively (Wang *et al.*, 2018). On the other hand, the small clay minerals contents, at least in comparison with COX and OPA clays, may lead to a reduced ability to seal cracks. Moreover, the Tamusu groundwater containing Ca^{2+} and Mg^{2+} may play an important role in the retention of selenite (Heberling *et al.*, 2014; Sun *et al.*, 2017), which indicates that Tamusu mudstone in groundwater conditions may be more effective at immobilizing Se-79 compared to Beishan granite (He *et al.*, 2019). Finally, the presence of carbonates might also contribute to the immobilization of Sr^{2+} (Dong *et al.*, 2018).

However, the advantages and disadvantages of the Tamusu mudstone compared to other DGR rocks remain to be assessed carefully in the future.

Hydraulic conductivity of mudstone

Determining the hydraulic properties of low-permeability environments is an arduous task due to operational constraints, equipment performance and the complex physical processes (Lavanchy *et al.*,

https://doi.org/10.1180/clm.2020.12 Published online by Cambridge University Press

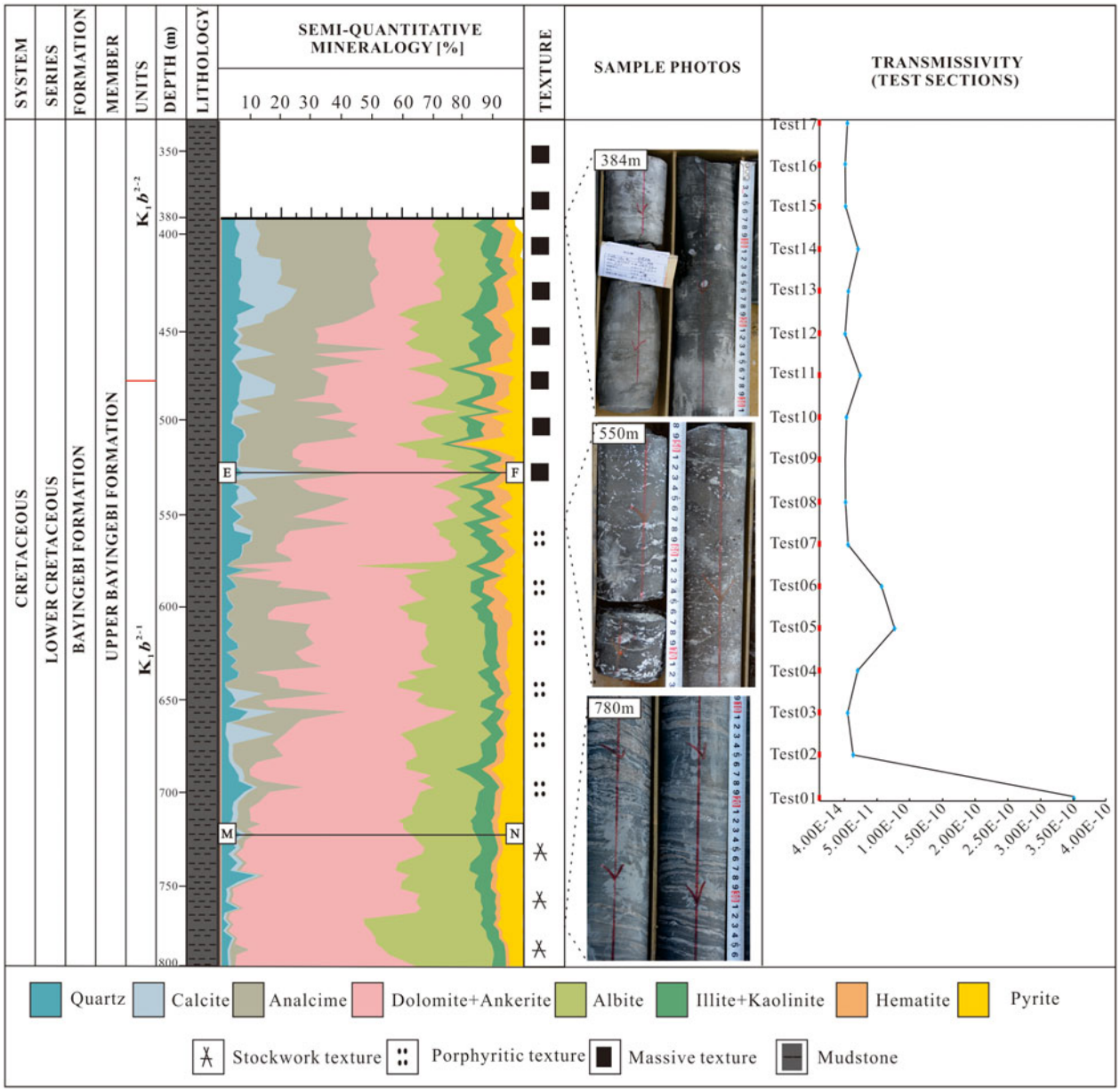

Fig. 7. Minerals and transmissivities of the samples from borehole TZK-2.

1998). The HDDP system has been used frequently in Beishan granite, and a relatively complete technical test scheme of borehole hydraulic conductivity has therefore been established, which effectively guarantees the smooth completion of pulse tests (Ji *et al.*, 2018). Furthermore, the applicable scales summarized from various test methods for low-permeability rocks indicate that the pulse tests have wider applicability to low-permeability formations, even in the range of 10^{-14}–10^{-9} m s^{-1} (Mejías, 2005). However, the 'skin effect' and short duration of a pulse test could not be avoided completely, and therefore these may affect the transmissivities obtained (Moench & Hsieh, 1985; Connell, 1994). To address this possibility, the test data were acquired between the point of closing the valve and executing the test after waiting for the system to stabilize over the course of several hours and up to several days. In addition, it is known that slight variations in the lower packer volume during a pulse test may increase the water head in the lower test sections (Fig. 9). For this reason, the observations in both the test section and the lower test sections were completed simultaneously during the pulse test. Some of these tests were conducted to confirm the proper operation of the instrumentation, and they included exposing the test valve to various pressures and using various types of pressure sensors. However, it was difficult to interpret the results of these limited tests. A total of 32 sets of pulse tests were conducted. These included 14 groups of tests for borehole TZK-1 to obtain 28 sets of transmissivities from 418.24 to 753.85 m and 18 groups of tests for borehole TZK-2 to obtain 24 sets of transmissivities from 280.85 to 712.21 m.

Hydraulic conductivity characteristics of borehole TZK-1

A total of 28 sets of transmissivity values were obtained from the test sections and the lower test sections. All of the transmissivities obtained were $<10^{-10}$ m^2 s^{-1} (Table 1), which could be converted to a hydraulic conductivity of $<10^{-12}$ m s^{-1} (the

https://doi.org/10.1180/clm.2020.12 Published online by Cambridge University Press

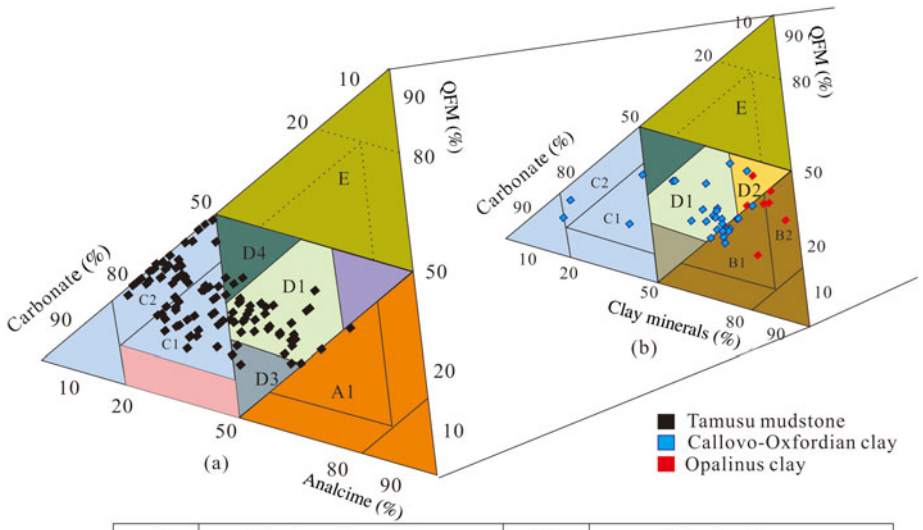

A1	Mixed analcime mudstone	D1	Mixed mudstone
B1	Mixed argillaceous mudstone	D2	Argillaceous/siliceous mudstone
B2	Silica-rich argillaceous mudstone	D3	Analcime/carbonate mudstone
C1	Mixed carbonate mudstone	D4	Carbonate/siliceous mudstone
C2	Silica-rich carbonate mudstone	E	Siliceous mudstone

Fig. 8. Classification triangle diagram of Tamusu mudstone, COX clay and OPA clay based on Zhong *et al.* (2018). (a) Tamusu data points; (b) COX and OPA data points. The COX clay data are from Gaucher (2004) and the OPA clay data are from Ould Bouya (2014). QFM = quartz + feldspar + mica.

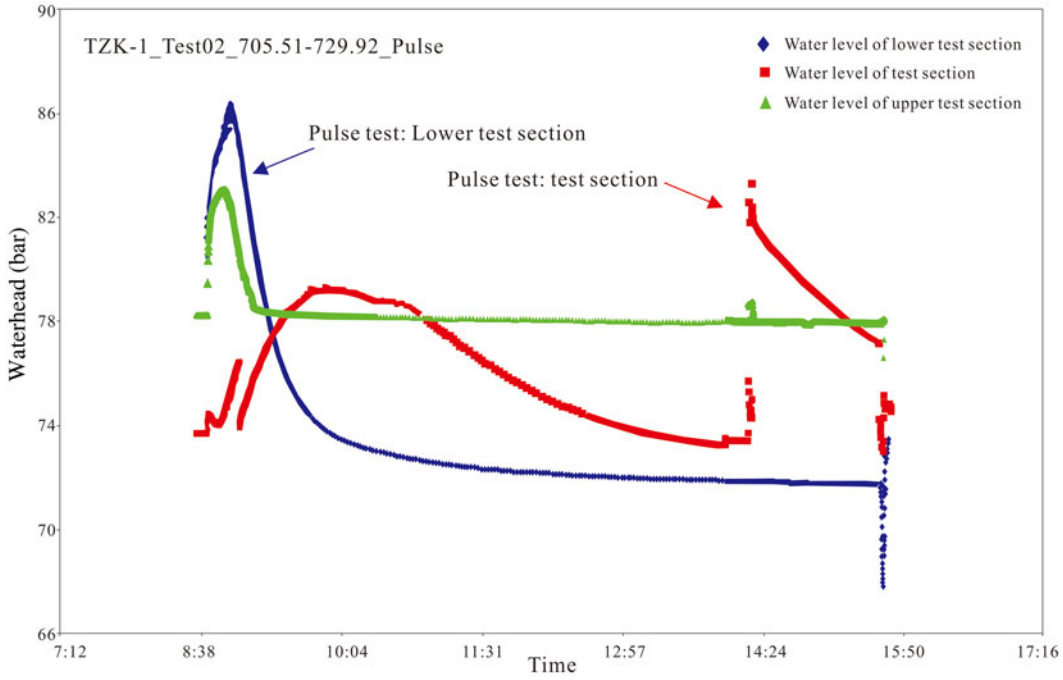

Fig. 9. Waterhead pressure–time response curve of Test02 in the test section of borehole TZK-1.

length of the test section was 24.41 m). The hydraulic conductivities in the test sections (Fig. 10a) and lower test sections (Fig. 10b) were typically $<10^{-11}$ m s^{-1}, but varied from 10^{-12} to 10^{-10} m s^{-1}. Based on the China Code for the Engineering Geological Investigation of Water Resources and Hydropower (GB50487-2008; Ministry of Water Resources, 2009), micro-permeability refers to rocks with hydraulic conductivities ranging from 10^{-8} to 10^{-7} m s^{-1}, and ultra-low permeability refers to rocks with hydraulic conductivities $<10^{-8}$ m s^{-1}. Therefore, it was concluded that the Tamusu mudstone in the test sections of borehole TZK-1 exhibited the characteristics of ultra-low-permeability rocks.

The transmissivities of test sections Test06 to Test01 from borehole TZK-1 were less, by nearly an order of magnitude, than test sections Test07–Test13. In particular, the test sections at <600 m had lower transmissivities than those of the interbedded structure of mudstone–sandstone–mudstone (Fig. 2), which indicates that the distinct lithology had a noticeable effect on the transmissivities, even though there were no visible changes in the transmissivities in the relatively consistent rock sections.

https://doi.org/10.1180/clm.2020.12 Published online by Cambridge University Press

Table 1. Transmissivities of the various test sections in borehole TZK-1.

Top (m)	Base (m)	Test section	T_TS (m^2 s^{-1})	T_LTS (m^2 s^{-1})
729.44	753.85	Test01	4.26E–12	7.60E–12
705.51	729.92	Test02	2.37E–12	5.30E–12
681.58	705.99	Test03	8.30E–12	3.60E–12
657.63	682.04	Test04	4.18E–12	1.41E–11
633.70	658.11	Test05	7.73E–12	2.12E–11
609.78	634.19	Test06	7.08E–13	1.40E–11
585.84	610.25	Test07	2.62E–11	2.36E–11
561.88	586.29	Test08	2.02E–11	2.31E–11
537.94	562.35	Test09	1.60E–11	8.98E–12
514.01	538.42	Test10	1.12E–11	1.10E–11
490.09	514.50	Test11	2.03E–11	1.62E–11
466.14	490.55	Test12	1.49E–11	1.45E–11
442.17	466.58	Test13	1.78E–11	1.83E–11
418.24	442.65	Test14	4.01E–12	2.57E–11

T_LTS = transmissivities of the lower test section; T_TS = transmissivities of the test section.

Table 2. Transmissivities of the various test sections in borehole TZK-2.

Top (m)	Base (m)	Test section	T_TS (m^2 s^{-1})	T_LTS (m^2 s^{-1})
687.78	712.21	Test01	3.52E–10	
663.82	688.25	Test02	1.32E–11	
639.90	664.33	Test03	4.64E–12	8.86E–14
615.96	640.39	Test04	2.02E–11	6.80E–11
592.04	616.47	Test05	7.62E–11	6.56E–11
568.10	592.54	Test06	5.66E–11	7.04E–11
544.16	568.59	Test07	5.38E–12	2.16E–11
520.22	544.66	Test08	1.30E–12	8.54E–11
496.27	520.70	Test09	4.22E–13	
472.33	496.76	Test10	2.83E–12	
448.39	472.82	Test11	2.40E–11	
424.47	448.90	Test12	1.26E–13	
400.52	424.96	Test13	6.10E–12	
376.59	401.02	Test14	2.05E–11	
352.66	377.09	Test15	1.18E–12	
328.72	353.15	Test16	7.08E–13	
304.79	329.22	Test17	4.44E–12	
280.85	305.28	Test18	4.10E–07	

T_LTS = transmissivities of the lower test section; T_TS = transmissivities of the test section.

Hydraulic conductivity characteristics of borehole TZK-2

The data obtained from borehole TZK-2 test sections were processed in the same way as those of borehole TZK-1, and the corresponding transmissivities were obtained from the lower test sections as the quality of the data there was higher. In total, 18 sets of transmissivities were obtained from the test sections and six sets were obtained from the lower test sections (Table 2).

Test section Test18 between 280.85 and 305.28 m in depth had a transmissivity of 4.1×10^{-7} m^2 s^{-1}, which is $>10^{-10}$ m^2 s^{-1} (Table 2), and may have been caused by a potentially silty mudstone formation. The transmissivities of the other test sections were $<10^{-10}$ m^2 s^{-1}, which correspond to hydraulic conductivities of $<10^{-11}$ m s^{-1} (length of test section: 24.43 m). Similarly to borehole TKZ-1, the borehole TZK-2 test sections contained rocks with ultra-low permeability. The hydraulic conductivity was typically 10^{-12} m s^{-1} and ranged from 10^{-13} to 10^{-9} m s^{-1}, which also indicates that the mudstone exhibited ultra-low permeability (Fig. 11a). It was confirmed that the rocks in the lower test sections were of ultra-low permeability, as the hydraulic conductivities ranged from 10^{-13} to 10^{-10} m s^{-1} (Fig. 11b). Hence, the pulse tests performed using the HDDP system confirmed the ultra-low permeability of the rock in the Tamusu mudstone. As the consistent lithology of the mudstone ranged from 300 to 700 m in borehole TZK-2, there were no visible fluctuations in the transmissivities with depth. Test sections from Test06 to Test01 had transmissivities that were an order of magnitude larger than those from Test17 to Test07, which indicates lower transmissivities in the latter test sections (from 304.79 to 568.10 m).

In 2014, exploratory experiments to determine the hydraulic conductivity of Tamusu mudstone were conducted using a rock mechanics test system (MTS815.04, MTS Systems Corporation, USA; Hu, 2014). These results are in agreement with those obtained in the present study. The hydraulic conductivity obtained via *in situ* tests is consistent with the published laboratory results. These hydraulic conductivity results are consistent with the values reported in the literature for argillaceous formations in other locations. For example, hydraulic conductivities were reported between 10^{-14} and 10^{-12} m s^{-1} for OPA and COX clays, respectively (Andra, 2005; Delay *et al.*, 2006; Distinguin & Lavanchy, 2007), and between 10^{-13} and 10^{-11} m s^{-1} for Toarcian argillite in Tournemire (Boisson *et al.*, 2001).

The transmissivities were compared with the mineralogical composition of the various rock types. The test sections with lower transmissivities were those mudstone samples that featured

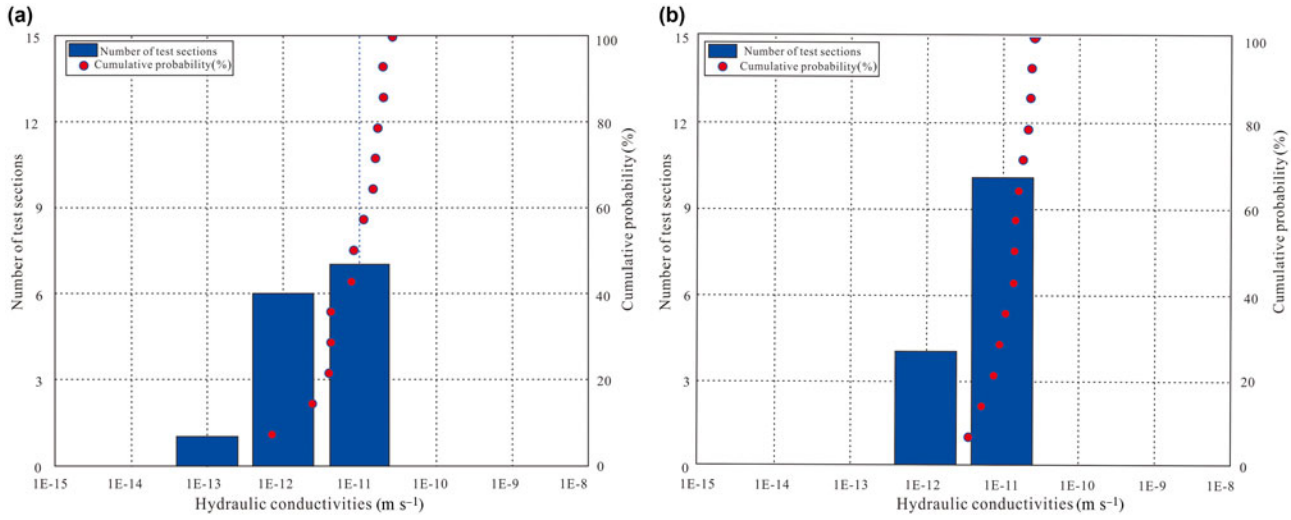

Fig. 10. Statistical chart of the hydraulic conductivities of the test sections in borehole TZK-1.

https://doi.org/10.1180/clm.2020.12 Published online by Cambridge University Press

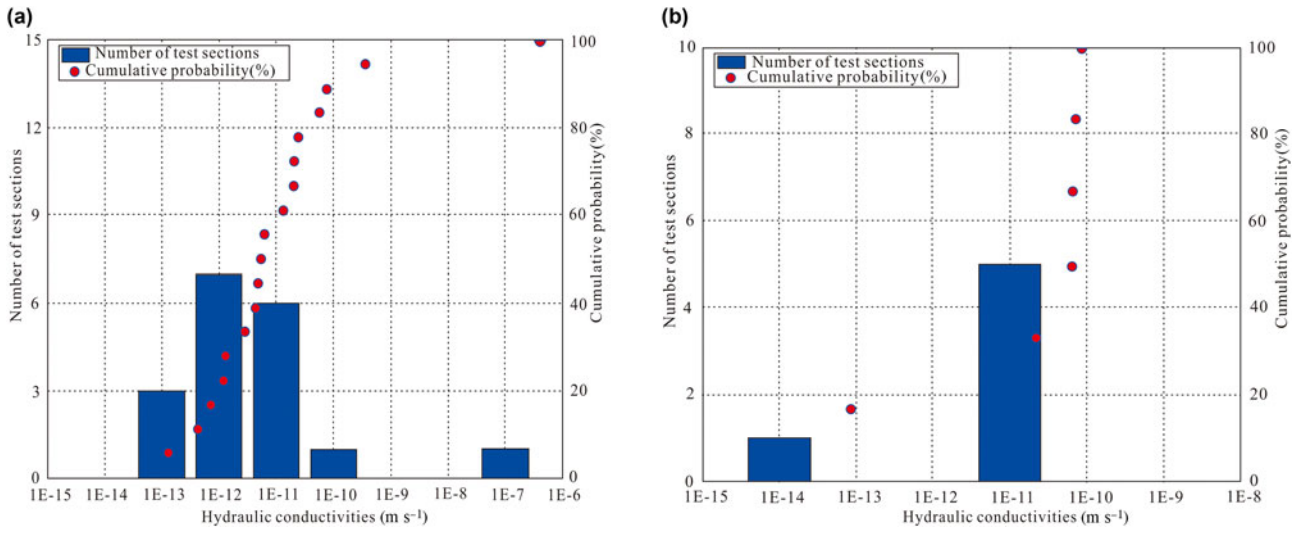

Fig. 11. Statistical chart of the hydraulic conductivities of the test sections in borehole TZK-2.

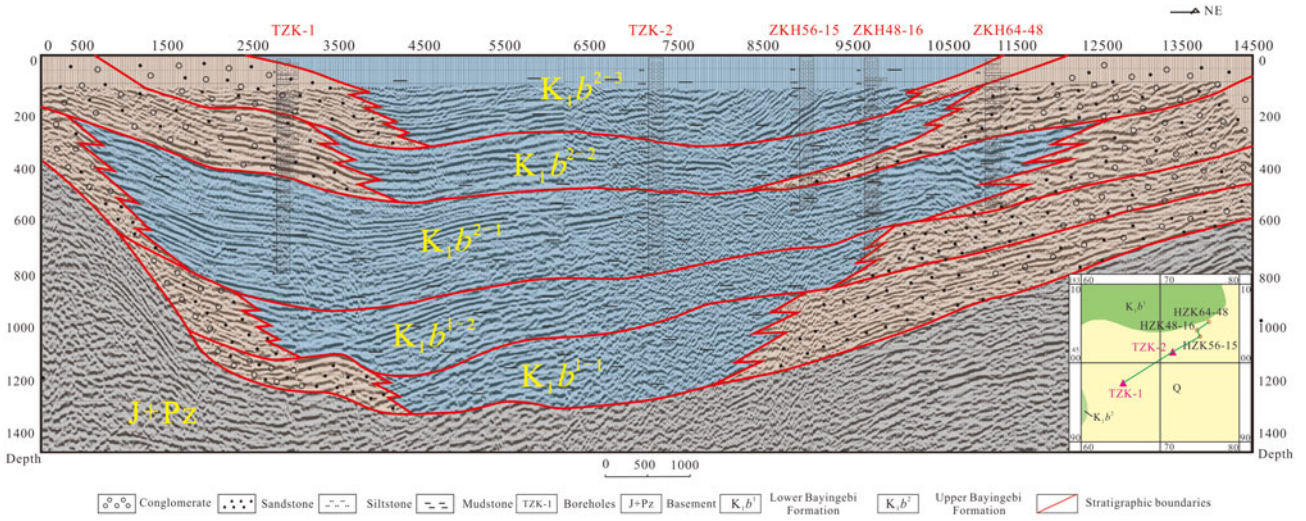

Fig. 12. Northeast–southwest well tie sections in the Tamusu candidate region. J+Pz = Jurassic + Palaeozoic.

massive structures and relatively high analcime mass fractions (mainly above Line E–F) (Fig. 7). The reason for this relationship is not known. Between 1994 and 2004, Andra collected hydraulic data related to argillite from deep boreholes obtained from short-term hydraulic packer tests and long-term monitoring of the formation pressures, which also confirmed that the hydraulic conductivity did not exhibit a distinct trend with depth for the COX clay (Distinguin & Lavanchy, 2007). It is often difficult to explain the various transmissivities because microstructural aspects have to be considered. The role of analcime with respect to the transmissivity of the Tamusu mudstone needs to be investigated further.

In general, in this ultra-low-permeability rock, an order of magnitude difference can be seen in the Tamusu mudstone transmissivities for varying lithologies, whereas no fluctuations were observed in the transmissivities for various depths for consistent lithology.

Spatial distribution conditions

The spatial distributions of mudstone in the upper Bayingebi Formation were analysed using well ties and shallow seismic profiles. The seismic data with calibrated stratigraphic boundaries were provided by the Remote Sensing Center of Nuclear Industry, China National Nuclear Corporation (CNNC). In combination with borehole lithology histograms from Geologic Party No. 208, the spatial distribution of mudstone can be determined by analysing the northeast–southwest well ties (Fig. 12). In particular, the semi-deep and deep lacustrine facies developed during the deposition of the first lithological unit (K_1b^{2-1}). Near the depositional centre of the basin, the entire borehole TZK-2 consists of dark grey mudstone. A layer of continuous grey mudstone was identified from the lithology histograms at a burial depth of between 500 and 800 m. Then, influenced by tectonic movements and a dryer climate during the deposition stages of the second (K_1b^{2-2}) and third lithological units (K_1b^{2-3}), the lacustrine basin shrank as clastic sediments were deposited, reflecting a fan delta front, braided delta plain sub-facies and a shallow lacustrine environment. It is worth noting that sections of grey mudstone were identified in the samples from boreholes TZK-2, ZKH56-15 and ZKH64-48 at burial depths of between 100 and 300 m. Based on the continuous thickness of the COX clay (130 m) in France and the OPA clay (131 m) in

https://doi.org/10.1180/clm.2020.12 Published online by Cambridge University Press

Switzerland (Mari & Yven, 2014; Bossart *et al.*, 2017), it was surmised that the thickness of the continuous target formation in the Tamusu area may be >300 m because of the unexposed base of the target formation (K_1b^2). More importantly, the spatial distribution (*i.e.* the continuous thickness and burial depth) was suitable as a host rock for a DGR.

Conclusions

1. The spatial distribution features of the target formation were determined to have a continuous thickness of >300 m and a suitable burial depth. The southwest margin and depositional centre were well delineated by boreholes TZK-1 and TZK-2, respectively.
2. Three main mineral types were identified in Tamusu mudstone (carbonates, analcime and albite) and three facies were distinguished based on mineral abundance. The Tamusu mudstone contains fewer clay minerals than the COX and OPA clays, but more carbonate phases, which may result in increased mechanical stability, but less potential for sealing cracks. Analcime may contribute to radionuclide immobilization by adsorption, at least of cationic radionuclides. The specific advantages and disadvantages resulting from the specific properties of the Tamusu mudstone remain to be assessed in the future.
3. The Tamusu mudstone was confirmed to consist of ultra-low-permeability rocks. Distinct lithologies may affect the hydraulic conductivity of the rock, although no fluctuations with depth were observed for consistent lithology.

Based on the results of this study, it was concluded that the target formation in Tamusu mudstone might be suitable as a host rock for the clay rock DGRs of China's HLRW. The findings of this work are expected to provide a solid basis for further assessment. In terms of future work, more parameters of Tamusu mudstone, such as adsorption, diffusion, swelling for closing cracks and mechanical workability, among others, remain to be investigated.

Acknowledgements. The authors are very grateful to the editors and two anonymous reviewers for their constructive comments and suggestions, which improved the paper significantly. They also express their gratitude to Geological Team No. 208 and the Remote Sensing Center of Nuclear Industry, CNNC, for their support and assistance during the field visit and data collection. In particular, they are grateful for the guidance with the XRD analysis to Dr Michel Cathelineau and Dr Daniele Bartier of the University of Lorraine.

Financial support. This publication was funded by the State Administration of Science, Technology and Industry for National Defense (Two Division of Technology and Industry, [2014] 1587), Jiangxi Province Graduate Innovation Funding Project (YC2018-B083) and Jiangxi Province Post-Doctoral Scientific Research Project (2018KY42).

References

Andra (2005) *Andra Research on the Geological Disposal of High-Level Long-Lived Radioactive Waste: Results and Perspectives*. French National Radioactive Waste Management Agency, Paris, France, 40 pp.

Andra (2015) Status of the Cigéo Project in France – French industrial geological disposal project. Presented at: *LUCOEX Conference and Workshop*, 2–4 June 2015, Oskarshamn, Sweden.

Bish D.L. (1999) Natural Zeolites and Nuclear-Waste Management: The Case of Yucca Mountain, Nevada, USA. Pp. 177–191 in: *Natural Microporous Materials in Environmental Technology*. Springer Netherlands, Dordrecht, The Netherlands.

Boisson J.Y., Bertrand L., Heitz J.F. & Moreau-le Golvan Y. (2001) *In situ* and laboratory investigations of fluid flow through an argillaceous formation at different scales of space and time, Tournemire tunnel, southern France. *Hydrogeology Journal*, **9**, 108–123.

Bossart P., Bernier F., Birkholzer J., Bruggeman C., Connolly P., Dewonck S. *et al.* (2017) Mont Terri rock laboratory, 20 years of research: introduction, site characteristics and overview of experiments. *Swiss Journal of Geosciences*, **110**, 3–22.

Charles N., Augier R., Gumiaux C., Monie P., Chen Y., Faure M. & Zhu R. (2013) Timing, duration and role of magmatism in wide rift systems: insights from the Jiaodong Peninsula (China, East Asia). *Gondwana Research*, **24**, 412–428.

Connell L.D. (1994) The importance of pulse duration in pulse test analysis. *Water Resources Research*, **30**, 2403–2411.

Cuss R.J., Harrington J.F., Giot R. & Auvray C. (2014) Experimental observations of mechanical dilation at the onset of gas flow in Callovo-Oxfordian claystone. *Geological Society London Special Publications*, **400**, 507–519.

Delay J., Lebon P. & Robours H. (2010) Meuse/Haute-Marne center: next steps towards a deep disposal facility. *Journal of Rock Mechanics and Geotechnical Engineering*, **2**, 52–70.

Delay J., Trouiller A. & Lavanchy J.M. (2006) Hydrodynamic properties of the Callovo-Oxfordian formation in the east of the Paris Basin: comparison of results obtained through different approaches. *Comptes Rendus – Academie des Sciences. Geoscience*, **338**, 892–907.

Deng J.Y. (2013) Discussion on sedimentary system and uranium metallogenic model of Upper Bayingebi Formation in Tamusu area. *World Nuclear Geoscience*, **30**, 86–90 (in Chinese with English abstract).

Distinguin M. & Lavanchy J.M. (2007) Determination of hydraulic properties of the Callovo-Oxfordian argillite at the Bure site: synthesis of the results obtained in deep boreholes using several in situ investigation techniques. *Physics and Chemistry of the Earth*, **32**, 379–392.

Dong Y., Wang H.L., Zhao S.W., He H.Y., Jia M.L., Liu J. *et al.* (2018) Adsorption of Sr^{2+} on dolomite and analcime. *Atomic Energy Science and Technology*, **52**, 1942–1948 (in Chinese with English abstract).

Dou L. & Chang L. (2003) Fault linkage patterns and their control on the formation of the petroleum systems of the Erlian Basin, Eastern China. *Marine and Petroleum Geology*, **20**, 1213–1224.

Gaucher E., Robelin C., Matray J.M., Negrel G., Gros Y., Heitz J.F. *et al.* (2004) ANDRA underground research laboratory: interpretation of the mineralogical and geochemical data acquired in the Callovian–Oxfordian formation by investigative drilling. *Physics and Chemistry of the Earth*, **29**, 55–77.

Guan W.C., Liu X.D. & Liu P.H. (2014) Study on the geological characteristics of claystone in Tamusu area of Bayingebi Basin. *World Nuclear Geoscience*, **31**, 95–102 (in Chinese with English abstract).

He H.Y., Jun L., Dong Y., Li H.H., Zhao S.W., Wang J. *et al.* (2019) Sorption of selenite on Tamusu clay in simulated groundwater with high salinity under aerobic/anaerobic conditions. *Journal of Environmental Radioactivity*, **203**, 210–219.

Heberling F., Vinograd V.L., Polly R., Gale J.D., Heck S., Rothe J. *et al.* (2014) A thermodynamic adsorption/entrapment model for selenium (IV) coprecipitation with calcite. *Geochemica et Cosmochimica Acta*, **134**, 16–38.

Hu H.Y. (2014) *Mechanical Properties of Clay Rocks from Tamusu Area*. Master's thesis, East China University of Technology, China (in Chinese with English abstract).

Hudson J.A., Cosgrove J.W., Kemppainen K. & Johansson E. (2011) Faults in crystalline rock and the estimation of their mechanical properties at the Olkiluoto site, western Finland. *Engineering Geology*, **117**, 246–258.

IAEA (1997) *Experience in Selection and Characterization of Sites for Geological Disposal of Radioactive Waste*. TECDOC-991. International Atomic Energy Agency, Vienna, Austria, 32 pp.

IAEA (2003) *Scientific and Technical Basis for Geological Disposal of Radioactive Wastes*. Technical Reports Series No. 413. International Atomic Energy Agency, Vienna, Austria, 80 pp.

Ji R.L., Zhang M., Zhou Z.C. & Li J.B. (2018) Research on *in-situ* hydraulic test method in Beishan pre-selected area. *Uranium Geology*, **34**, 53–59 (in Chinese with English abstract).

Kohno M., Nara Y., Kato M. & Nishimura T. (2018) Effects of clay-mineral type and content on the hydraulic conductivity of bentonite–sand mixtures made of Kunigel bentonite from Japan. *Clay Minerals*, **53**(4), 721–732.

Lavanchy J.M., Croise J., Tauzin E. & Eilers G. (1998) Hydraulic testing in low permeability formations. Test design, analysis procedure and tools. Application from

https://doi.org/10.1180/clm.2020.12 Published online by Cambridge University Press

a site characterization programme. Presented at: *International Conference on Radioactive Waste Disposal*, 9–11 September 1998, Hamburg, Germany.

Li H., Liu Y.Q. & Liang H. (2012) Lithology and origin analysis of sublacustrine hydrothermal deposits characterized by analcime, sanidine, dolomite, quartz, etc in Lucaogou Formation, Middle Permian, Santanghu Basin, northeast Xinjiang, China. *Acta Sedimentologica Sinica*, **30**(2), 205–218 (in Chinese with English abstract).

Li P. (2018) *Study on Uranium Mineralization and Prospecting Prediction in Tamusu Area of Alxa Youqi, Inner Mongolia*. Master's thesis, Ji Lin University, China (in Chinese with English abstract).

Lin C., Eriksson K., Li S., Wan Y., Ren J. & Zhang Y. (2001) Sequence architecture, depositional systems, and controls on development of lacustrine basin fills in part of the Erlian basin, northeast China. *AAPG Bulletin*, **85**, 2017–2043.

Liu X.D. & Liu P.H. (2012) The basic features of clay rock in Tamusu area. Pp. 50–58 in *Papers of the Fourth Academic Seminar on Underground Waste Disposal* (in Chinese with English abstract). Waste Underground Disposal Committee of Chinese Society of Rock Mechanics and Engineering, Nanchang, China.

Liu X.D., Liu P.H., Wang C.X. & Che S. (2010) Preliminary sitting of clay formations for HLW geological depository in China. Pp. 117–127 in *Papers of the Third Academic Seminar on Underground Waste Disposal* (in Chinese with English abstract). Waste Underground Disposal Committee of Chinese Society of Rock Mechanics and Engineering, Hangzhou, China.

Mari J.L. & Yven B. (2014) The application of high-resolution 3D seismic data to model the distribution of mechanical and hydrogeological properties of a potential host rock for the deep storage of radioactive waste in France. *Marine and Petroleum Geology*, **53**, 133–153.

Matusewicz M. & Olin M. (2019). Comparison of microstructural features of three compacted and water-saturated swelling clays: MX-80 bentonite and Na- and Ca-purified bentonite. *Clay Minerals*, **54**, 75–81.

Mazurek M., Gautschi A., Marschall P., Vigneron G., Lebon P. & Delay J. (2008) Transferability of geoscientific information from various sources (study sites, underground rock laboratories, natural analogues) to support safety cases for radioactive waste repositories in argillaceous formations. *Physics and Chemistry of the Earth*, **33**, 95–105.

McEvoy F.M., Schofield D.I., Shaw R.P. & Norris S. (2016) Tectonic and climatic considerations for deep geological disposal of radioactive waste: a UK perspective. *Science of the Total Environment*, **571**, 507–521.

McMaster S.A., Ram R., Faris N. & Pownceby M.I. (2018) Radionuclide disposal using the pyrochlore supergroup of minerals as a host matrix – a review. *Journal of Hazardous Materials*, **360**, 257–269.

Mejías M. (2005) Hydraulic testing of low-permeability fractured rocks: methodology and comparative analysis. Presented at: *7th Hellenic Hydrogeology Conference and 2nd Workshop on the Hydrogeology of Fissured Rocks*, Athens, Greece.

Meng Q.R., Hu J.M., Yuan X.J. & Jin J.Q. (2002) Structure, evolution and origin of Late Mesozoic extensional basins in the China–Mongolia border region. *Geological Bulletin of China* **21**, 224–231 (in Chinese with English abstract).

Ministry of Water Resources of the People's Republic of China (2009) *GB50487-2008 Code for Engineering Geological Investigation of Water Resources and Hydropower*. China Planning Press, Beijing, China.

Misaelides P. (2019) Clay minerals and zeolites for radioactive waste immobilization and containment. Pp. 243–274 in *Modified Clay and Zeolite Nanocomposite Materials*. Elsevier, Amsterdam, The Netherlands.

Moench A.F. & Hsieh P.A. (1985) Comment on 'Evaluation of slug tests in wells containing a finite-thickness skin' by C.R. Faust and J.W. Mercer. *Water Resources Research*, **21**, 1459–1461.

NAGRA (2002) *Project Opalinus Clay: models, codes and data for safety assessment-edemonstration of disposal feasibility for spent fuel, vitrified high-level waste and long-lived intermediate-level waste*. Technical report. National Cooperative for the Disposal of Radioactive Waste, Wettingen, Switzerland, 504 pp.

NEA (2001) *The Role of Underground Laboratories in Nuclear Waste Disposal Programs*. Organisation for Economic Co-operation and Development (OECD), Paris, France.

Ould Bouya M.L. (2014). *Acquisition d'un profil de perméabilité intrinsèq ue au sein de l'Argile à Opalines du Mont Terri par analyse minéralogique et pétrophysique*. Master's thesis, Université Paris-Sud 11, Orsay, France (in French).

Pan Z.Q. & Qian Q.H. (2009) *Strategy Research on High-Level Radioactive Waste Geological Disposal*. Publishing House of Atomic Energy, Beijing, China (in Chinese), pp. 15–17.

Reynolds R.C. (1989) Principles and techniques of quantitative analysis of clay minerals by X-ray powder diffraction. Pp. 3–36 in *CMS Workshop Lecture Series, Vol. I. Quantitative Mineral Analysis of Clays* (D.R. Pevear & F.A. Mumpton, editors). Clay Minerals Society, Boulder, CO, USA.

Sasamoto H., Isogai T., Kikuchi H., Satoh H. & Svensson D. (2017) Mineralogical, physical and chemical investigation of compacted Kunigel V1 bentonite in contact with a steel heater in the ABM test unit 1 experiment, Äspö Laboratory, Sweden. *Clay Minerals*, **52**, 127–142.

SKB (2004) *R&D Programme 2004: Programme for Research, Development and Demonstration of Methods for the Management and Disposal of Nuclear Waste Including Social Science Research*. TR-04-21. Swedish Nuclear Fuel and Waste Management Co. (SKB), Stockholm, Sweden, 412 pp.

Sun W., Renew J.E., Zhang W., Tang Y. & Huang C.H. (2017) Sorption of Se (IV) and Se (VI) to coal fly ash/cement composite: effect of Ca^{2+} and high ionic strength. *Chemical Geology*, **464**, 76–83.

Thierry H. (1985) *Les minéraux argileux: préparation, analyse diffractométrique et détermination*. Société géologique du Nord, Villeneuve d'Ascq, France (in French), 136 pp.

Wang F.G., Hou S.R., Zhang L., Men H. & Wang J.L. (2018) Study on the characteristics of water–rock interaction and its relation to uranium mineralization in Tamusu uranium deposit, southern Bayin Gobi Basin. *Geological Review*, **64**, 633–646 (in Chinese with English abstract).

Wang J., Chen L., Su R. & Zhao X.G. (2018) The Beishan underground research laboratory for geological disposal of high-level radioactive waste in China: planning, site selection, site characterization and in situ tests. *Journal of Rock Mechanics and Geotechnical Engineering*, **10**, 411–435.

Wang Y., Liang H.A., Hu Q.B., Chen H.K., Wang C. & Xie Z. (2018) Study on correlation between mineral composition and elastic modulus of clay rock in Tamusu. *Chongqing Architecture*, **17**, 18–21 (in Chinese with English abstract).

Wei H.Y. & Jiang, X.C. (2019) Early Cretaceous ferruginous and its control on the lacustrine organic matter accumulation: constrained by multiple proxies from the Bayingebi Formation in the Bayingebi Basin, Inner Mongolia, NW China. *Journal of Petroleum Science and Engineering*, **178**, 162–179.

Wei P.S., Zhang H.Q. & Chen, Q.L. (2006) *Petroleum Geological Characteristics and Exploration Prospects in the Yingen-Ejinaqi Basin*. Petroleum Industry Press, Beijing, China (in Chinese), pp. 50–51.

Wu R.G., Zhou W.P., Xu Z., Liu P.H. & Zhang L. (2010) Discussion on the chronology of Suhongtu Forrnation in Bayingebi Basin. *Uranium Geology*, **26**(3), 152–157 (in Chinese with English abstract).

Yang Y.Y., Liu X.D., Liu P.H. & Xiang L. (2017) Evaluation of clay rock preselected site of high-level radioactive waste repository based on analytic hierarchy process: a case study of Tamusu region and Longdong area. *Resources Environment & Engineering*, **31**, 601–605 (in Chinese with English abstract).

Yoshida H., Nagatomo A., Oshima A. & Metcalfe R. (2014) Geological characterization of the active Atera Fault in central Japan: implications for defining fault exclusion criteria in crystalline rocks around radioactive waste repositories. *Engineering Geology*, **177**, 93–103.

Zhang C.L. (2018) Thermo-hydro-mechanical behavior of clay rock for deep geological disposal of high-level radioactive waste. *Rock Mechanics and Geotechnical Engineering*, **10**, 992–1048.

Zhang C.L., Wang J. & Su K. (2006) Concepts and tests for disposal of radioactive waste in deep geological formations. *Chinese Journal of Rock Mechanics and Engineering*, **25**, 750–767.

Zhang C.Y., Nie F.J., Jiao Y.Q., Deng W., Peng Y.B., Hou S.R. *et al.* (2019) Characterization of ore-forming fluids in the Tamusu sandstone-type uranium deposit, Bayingobi Basin, China: constraints from trace elements, fluid inclusions and C–O–S isotopes. *Ore Geology Reviews*, **2019**, 102999.

Zhong D.K., Yang Z., Sun H.T. & Zhang S. (2018) Petrological characteristics of hydrothermal-sedimentary rocks: a case study of the Lower Cretaceous Tengger Formation in the Baiyinchagan sag of Erlian Basin, Inner Mongolia. *Journal of Paleogeography*, **20**(1), 20–32 (in Chinese with English abstract).

Zhou J.B., Wilde S.A., Zhang X.Z., Ren S.M. & Zheng C.Q. (2010) Early Paleozoic metamorphic rocks of the Erguna block in the Great Xing'an Range, NE China: evidence for the timing of magmatic and metamorphic events and their tectonic implications. *Tectonophysics*, **12**, 50–78.

https://doi.org/10.1180/clm.2020.12 Published online by Cambridge University Press